

Structural and dynamic properties of liquid tin from a new modified embedded-atom method force field

Joseph R. Vella,¹ Mohan Chen,² Frank H. Stillinger,³ Emily A. Carter,⁴ Pablo G. Debenedetti,¹ and Athanassios Z. Panagiotopoulos^{1,*}

¹*Department of Chemical and Biological Engineering, Princeton University, Princeton, New Jersey 08544, USA*

²*Department of Mechanical and Aerospace Engineering, Princeton University, Princeton, New Jersey 08544, USA*

³*Department of Chemistry, Princeton University, Princeton, New Jersey 08544, USA*

⁴*School of Engineering and Applied Science, Princeton University, Princeton, New Jersey 08544, USA*

(Received 21 October 2016; revised manuscript received 21 December 2016; published 1 February 2017)

A new modified embedded-atom method (MEAM) force field is developed for liquid tin. Starting from the Ravelo and Baskes force field [*Phys. Rev. Lett.* **79**, 2482 (1997)], the parameters are adjusted using a simulated annealing optimization procedure in order to obtain better agreement with liquid-phase data. The predictive capabilities of the new model and the Ravelo and Baskes force field are evaluated using molecular dynamics by comparing to a wide range of first-principles and experimental data. The quantities studied include crystal properties (cohesive energy, bulk modulus, equilibrium density, and lattice constant of various crystal structures), melting temperature, liquid structure, liquid density, self-diffusivity, viscosity, and vapor-liquid surface tension. It is shown that although the Ravelo and Baskes force field generally gives better agreement with the properties related to the solid phases of tin, the new MEAM force field gives better agreement with liquid tin properties.

DOI: [10.1103/PhysRevB.95.064202](https://doi.org/10.1103/PhysRevB.95.064202)

I. INTRODUCTION

Tin has played a significant role in the course of human history. It is an essential component of bronze which saw widespread use throughout the world during the Bronze Age (around 3300–1200 BC). During this time, the creation of tools, weapons, and ornaments utilized bronze and therefore relied on tin. Humans needed to possess some understanding of the properties of liquid tin in order to create the bronze used in these artifacts. The necessity to understand liquid tin still holds today as evidenced by its importance in many modern technologies. For example, knowledge of liquid tin properties is useful for soldering. Soldering is important in several applications such as electronics, plumbing, and jewelry. Tin-lead alloys are common solders; however, environmental and ecological concerns sparked a search for lead-free solders especially when certain policies, such as the Waste Electrical and Electronic Equipment Directive which limits the use of lead in electronics, were implemented. Many alternative candidate alloys still contain tin as one of the main components [1,2]. Examples include binary alloys such as tin-copper, tin-silver, tin-gold, tin-zinc, tin-bismuth, and tin-indium [3] or even ternary alloys such as tin-silver-copper [4].

Liquid metals, including liquid tin and lithium-tin alloys [5–7], are currently being considered as alternative plasma-facing materials in tokamak fusion reactors for several reasons, such as the fact that liquid walls can self-replenish and they offer easier means of remote maintenance [6,8]. An understanding of the properties of these liquid metals is also needed in order to properly assess their potential use as plasma-facing materials. Relevant liquid metal properties include viscosities, diffusivities, hydrogen solubilities, and wetting properties. Recently, experimental studies have been performed focusing on the understanding of properties of liquid lithium [9,10] and

liquid tin [11,12] in the context of plasma-facing materials. Unfortunately, experimental studies on these properties, at conditions of interest, are not complete, especially for lithium-tin alloys. In addition, the effect of impurities in experiments can be significant, which complicates the understanding of the behavior of pure materials. For instance, oxygen impurities were reported to have significant effects on properties of lithium droplets [13] and tin thin films [14] on molybdenum surfaces. Computational studies for liquid metals can provide predictions where experimental data are lacking and also eliminate the effect of impurities on phenomena relevant to plasma-facing applications. One example is studying how liquid metals behave when bombarded with high-energy particles that escape the plasma in a tokamak reactor. An accurate computational approach to studying liquid tin would also be useful for examining various aspects of tin-based solders.

First-principles quantum mechanics (QM) methods, such as Kohn-Sham density functional theory [15,16], are widely used to simulate solid materials. However, these methods are computationally demanding for simulating liquids. In particular, QM methods cannot simulate very large system sizes or access long times. Many of the properties calculated in this work require system sizes of thousands of atoms and simulation times on the order of several nanoseconds. These size and time scales are not easily accessed using QM approaches. For example, the calculation of viscosity typically requires simulation times on the order of tens of nanoseconds. Classical molecular dynamics is an alternative method that can overcome these difficulties. However, it requires the specification of an interatomic force field to describe the interactions between atoms. The embedded-atom method (EAM) force fields [17] are widely used to simulate metallic systems. The modified embedded-atom method (MEAM) force fields [18] represent an extension of the EAM framework in which directional bonding is included in order to accurately describe different local structures, thus allowing

*Corresponding author: azp@princeton.edu

these models to be applied to a wider range of materials. Before these potentials can be used to predict properties relevant to plasma-facing or soldering applications, careful development and validation of the potentials needs to be done. This has already been performed for lithium EAM and MEAM force fields, by examining predictions for various coexistence and liquid properties [19,20]. In these studies it was shown that a lithium force field developed by Cui *et al.* [21] gave accurate predictions for several liquid-phase properties. A tin MEAM force field that accurately predicts liquid-phase properties would be useful not only for examining pure tin, but could also be used to study the liquid phase of lithium-tin alloys and the wetting properties of tin on solid substrates used in tokamak reactors. The tin force field could also be combined with other EAM force fields developed for different metals to investigate various tin alloys for their potential use as solder.

In this work, we present a critical evaluation of both an existing and new MEAM force field using geometry optimization and molecular dynamics. The existing tin force field was developed in 1997 by Ravelo and Baskes [22]. Although it performs well for the solid phases of tin, we show that it is not optimal for the liquid phase. We develop the second force field by tuning the parameters of the Ravelo and Baskes potential using a simulated annealing procedure with the goal of obtaining better agreement with liquid properties. For each force field, we calculate the cohesive energy, bulk modulus, and equilibrium volume of several crystal structures. We also calculate the melting temperature, density of the liquid phase, liquid-phase radial distribution functions, self-diffusivity, viscosity, and vapor-liquid surface tension. In each case, we compare the properties obtained from force fields to available experimental or QM data to assess the performance of each of the models.

We note that there are several other tin force fields available in the literature that we did not consider in this work. For example, an EAM force field was developed for the high-pressure crystal phases of tin [23]; however, we are not concerned with these phases in this work. Several studies utilize pair potentials (as opposed to the many-body EAM formalism) to study liquid tin [24–27]. These were not used in this work because it is known that treating metallic systems with a single pair potential cannot cover a wide range of conditions. This is illustrated in work by Canales *et al.* [28] in which the authors developed effective pair potentials for liquid lithium but mentioned that the potentials are dependent on the thermodynamic conditions being simulated. This is not practical for our purposes because we aim to study liquid tin over a broad range of temperatures and developing a new effective pair potential for each temperature would be cumbersome. There also exists work in which a nickel-tin MEAM potential was developed using the Ravelo and Baskes tin force field with one parameter changed [29]. However, this slightly modified Ravelo and Baskes force field was not examined in this work.

This paper is organized as follows. Section II reviews the MEAM model and the optimization procedure used to develop the new tin MEAM force field. Section III discusses the computational methods used to calculate various properties of solid and liquid tin. Section IV presents and discusses the results. Finally, Sec. V concludes the paper by summarizing

our findings and outlines the strengths and drawbacks of each tin MEAM force field.

II. MODEL AND OPTIMIZATION PROCEDURE

A. MEAM force field

The potential energy in the MEAM framework is given by

$$E_{\text{pot}} = \sum_j G_j(\phi_j) + \frac{1}{2} \sum_j \sum_{k \neq j} \varphi_{jk}(r_{jk}). \quad (1)$$

The term G_j is called the embedding energy and is a function of the effective electron density ϕ_j at the site of atom j . G_j can be interpreted as the energy it takes to embed atom j into an effective background electron density ϕ_j (which is due to the surrounding atoms). The embedding energy accounts for metallic bonding. The next term, $\varphi_{jk}(r_{jk})$, is a pair potential, which accounts for effective electrostatic interactions between atoms j and k with r_{jk} being the distance between them.

In the MEAM formalism, the embedding energy, effective background electron density, and pair potential are complicated functions containing many parameters. These parameters can be varied to give agreement to experimental and QM data. For the sake of brevity, we will not reproduce the forms of the aforementioned functions but will point the reader to a resource that provides this information [30]. We note that there is one occurrence where the form of a specific function differs between the Ravelo and Baskes force field and the new force field presented in this work. This appears in one of the contributions, $\phi_j^{(3)}$, to the effective background electron density (Eq. (4.7d) in Gullet *et al.* [30]). The new MEAM force field developed here takes the following form for this function:

$$\begin{aligned} (\phi_j^{(3)})^2 = & \sum_{x,y,z} \left[\sum_{k \neq j} \frac{r_{jk}^x r_{jk}^y r_{jk}^z}{r_{jk}^3} \phi_k^{a(3)}(r_{jk}) S_{jk} \right]^2 \\ & - \frac{3}{5} \sum_x \left[\sum_{k \neq j} \frac{r_{jk}^x}{r_{jk}} \phi_k^{a(3)}(r_{jk}) S_{jk} \right]^2, \end{aligned} \quad (2)$$

while the Ravelo and Baskes force field uses

$$(\phi_j^{(3)})^2 = \sum_{x,y,z} \left[\sum_{k \neq j} \frac{r_{jk}^x r_{jk}^y r_{jk}^z}{r_{jk}^3} \phi_k^{a(3)}(r_{jk}) S_{jk} \right]^2, \quad (3)$$

where the x , y , and z superscripts denote their respective components of the r_{jk} vector. $\phi_k^{a(3)}$ is a radial function that describes part of the contribution of atom k to the effective electron density at the site of atom j . S_{jk} is the value of the screening function for the interaction between atoms j and k . Equation (2) is used in more recent MEAM force fields in order to make the contributions to the effective background electron density orthogonal to one another [31].

Both force fields were implemented using the LAMMPS simulations package (15 May 2015 version) [32]. We note that the screening function implemented in LAMMPS [30] differs from the one used in the original Ravelo and Baskes paper. The screening function implemented by Ravelo and Baskes was outlined in a 1994 paper by Baskes *et al.* [33]. However, we were able to reproduce the reported α -tin (cubic diamond)

TABLE I. MEAM Parameters for the tin force fields examined in this work.

	Ravelo and Baskes [22]	New MEAM
E_c	3.08	3.06
r_{lat}^a	4.860	4.794
α	6.20	6.11
A	1.00	1.01
$\beta^{(0)}$	6.20	6.33
$\beta^{(1)}$	6.00	6.04
$\beta^{(2)}$	6.00	4.69
$\beta^{(3)}$	6.00	5.92
$t^{(0)}$	1.00	1.00
$t^{(1)}$	4.50	4.51
$t^{(2)}$	6.50	6.50
$t^{(3)}$	-0.183	0.029
C_{min}	0.8	0.8
C_{max}	2.8	2.8
r_c	5.5	4.8
Δr	0.1	0.2

^aThis is the lattice constant of the reference structure (which LAMMPS takes as an input).

and β -tin crystal energies and equilibrium volumes at 0 K and therefore concluded that the different screening function did not have a large effect on the properties calculated in this work. Both MEAM force fields in this work use the face-centered cubic (fcc) crystal as the reference structure. Although tin includes 10 stable isotopes, our calculations have assigned a common mass to all particles, where that assigned mass is an average determined by the natural occurrence frequencies of those isotopes (118.71 atomic mass units).

The MEAM parameters for the Ravelo and Baskes force field and the force field developed in this work are shown in Table I. It should be noted that many of the parameters of the new MEAM force field are very similar to the parameters of the Ravelo and Baskes force field. This is largely due to the fact that the Ravelo and Baskes parameters were used as a starting point for the optimization. In our attempt to accurately capture both solid and liquid properties of tin, most parameters were kept close to their initial values. More optimization details are provided in the next subsection. The LAMMPS files implementing these force fields are available as Supplemental Material [81].

B. Optimization of new MEAM force field

Here we describe the steps used to generate the new tin MEAM force field. The initial parameters of the MEAM force field were taken from the Ravelo and Baskes potential [22] with the exception of the cutoff distance (r_c) and the length of the smoothing distance for the cutoff function (Δr). Both r_c and Δr were chosen to match those used for the lithium MEAM force field of Cui *et al.* [21]. This was done for the convenience of the future development of cross parameters for lithium-tin alloys because LAMMPS defines a universal value of r_c and Δr for all species in alloy systems.

The target function is composed of both solid and liquid tin properties in an attempt to create a more robust and accurate

force field that captures properties of different phases of tin. The target function is defined as

$$\prod(\mathbf{x}) = \sum_{i=1}^N w_i |y_i - f_i(\mathbf{x})|, \quad (4)$$

where w_i is a weight factor and y_i is a target value for the i th physical property of tin. The target value for a given property is taken from either simulations or experiments. $f_i(\mathbf{x})$ is the same property obtained with a trial set of MEAM parameters \mathbf{x} . N is the total number of physical properties used in the optimization procedure. It is our goal to obtain a parameter set that produces a force field that yields predictions in agreement with the target values. This is equivalent to minimizing the target function. Eleven parameters were optimized, E_c , r_{lat} , α , A , $\beta^{(0)}$, $\beta^{(1)}$, $\beta^{(2)}$, $\beta^{(3)}$, $t^{(1)}$, $t^{(2)}$, and $t^{(3)}$. The other five parameters, C_{min} , C_{max} , $t^{(0)}$, r_c , and Δr , were fixed. The reason for fixing r_c and Δr has already been explained. C_{min} and C_{max} were fixed for both simplicity and because the values chosen are known to be appropriate for a MEAM force field that uses an fcc crystal as the reference structure. As pointed out by Baskes, $t^{(0)}$ can be set to unity without loss of generality [18]. The target function is composed of three contributions that are specified below. Simulated annealing was used to minimize the target function [34]. All of the properties used in the optimization procedure along with their contributions to the target function and reference data are outlined in Table II.

The first contribution includes properties of α -tin, β -tin, and the simple cubic (sc) solid crystal structures, specifically, the cohesive energies E_c , equilibrium volumes V_0 , and bulk moduli B_0 of these crystal structures at 0 K. The target values chosen for these properties are given here. For α -tin, we use -3.14 eV as the target cohesive energy [35], $34.05 \text{ \AA}^3/\text{atom}$ as the equilibrium volume [37], and 42.617 GPa as the bulk modulus from experiments [36]. Several different values for the energy difference between α -tin and β -tin at 0 K are available in the literature. For example, Ihm and Cohen [38] show that β -tin has a cohesive energy 0.04 eV/atom higher than α -tin from density functional theory calculations using the Wigner interpolation formula [40] for electron exchange and correlation, while Cheong and Chang [41] report a difference of 0.034 eV/atom using the local density approximation for electron exchange and correlation. Ihm and Cohen [38] also report that β -tin has a cohesive energy 0.015 eV/atom higher than α -tin based on experimental data. We choose the energy difference reported by Ihm and Cohen [38] from their density functional theory calculations. This gives a target cohesive energy of -3.10 eV/atom for β -tin. This was done in order to give a clear distinction between the cohesive energies of α -tin, β -tin, and the theoretical sc crystal structure. The equilibrium volume, $27.07 \text{ \AA}^3/\text{atom}$ [37], and bulk modulus, 57.037 GPa [36], for β -tin were taken from experiments. For each crystal structure, the lattice spacing was varied until the energy minimum was found. From this analysis the three aforementioned properties could be calculated. It is important to note that β -Sn has an anisotropic crystal structure which results in two independent lattice parameters. Due to the fact that the cohesive energy, equilibrium volume, and bulk modulus depend on the two independent lattice parameters,

TABLE II. Target functions utilized in tuning tin MEAM force fields. E_c , B_0 , V_0 , P_0 , and D_0 correspond to the cohesive energy (in eV/atom), bulk modulus (in GPa), equilibrium volume (in $\text{\AA}^3/\text{atom}$), pressure (in GPa), and diffusion coefficient (in $\text{\AA}^2/\text{ps}$), respectively. The reference values are from experiment (EXP), quantum mechanics (QM) calculations, or classical calculations using the Ravelo and Baskes potential. Weights for each component of the target function are also shown.

System	T (K)	Property	Target Function	Reference Value
α -tin	0	E_c	$1.0 \times -3.14 - E_c $	-3.14 eV/atom (EXP [35])
		B_0	$0.05 \times 42.617 - B_0 $	42.617 GPa (EXP [36])
		V_0	$0.01 \times 34.05 - V_0 $	$34.05 \text{\AA}^3/\text{atom}$ (EXP [37])
β -tin	0	E_c	$1.0 \times -3.10 - E_c $	-3.10 eV/atom (QM [38])
		B_0	$0.05 \times 57.037 - B_0 $	57.037 GPa (EXP [36])
		V_0	$0.10 \times 27.07 - V_0 $	$27.07 \text{\AA}^3/\text{atom}$ (EXP [37])
sc-tin	0	E_c	$1.0 \times -3.08 - E_c $	-3.08 eV/atom (Ravelo <i>et al.</i> [22])
		B_0	$0.05 \times 59.0 - B_0 $	59.0 GPa (Ravelo <i>et al.</i> [22])
		V_0	$0.01 \times 28.48 - V_0 $	$28.48 \text{\AA}^3/\text{atom}$ (Ravelo <i>et al.</i> [22])
NVT-MD ^a	773	P_0	$1.0 \times P_0 $	0.0 GPa
		D_0	$20.0 \times 0.50 - D_0 $	$0.50 \text{\AA}^2/\text{ps}$ (EXP [39])
	1273	P_0	$1.0 \times P_0 $	0.0 GPa
		D_0	$20.0 \times 1.10 - D_0 $	$1.10 \text{\AA}^2/\text{ps}$ (EXP [39])
NPT-MD ^b	580	D_0	$20.0 \times D_0 $	$0.0 \text{\AA}^2/\text{ps}$
	610	D_0	$20.0 \times D_0 $	$0.0 \text{\AA}^2/\text{ps}$
	640	D_0	$20.0 \times D_0 $	$0.0 \text{\AA}^2/\text{ps}$

^aSimulation of 216 liquid tin atoms for 5 ps with a time step of 1.0 fs.

^bSimulation of 216 solid β -tin atoms for 10 ps with a time step of 2.0 fs.

calculation of the contribution of β -tin to the objective function becomes more complicated when compared to the α -tin and simple cubic crystal structures. To get around this, during the optimization we only varied the larger lattice parameter and kept the ratio of the independent lattice parameters constant. We chose the ratio of the two lattice parameters (small to large) to be 0.546, which is taken from an experimental value [37]. We will refer to the larger lattice parameter of the β -tin structure as a and the smaller lattice parameter as c . It was found that this constraint on the optimization still yielded reasonable results for β -tin. For the simple cubic crystal structure, target values were set to those calculated using the Ravelo and Baskes force field because of a lack of experimental data. The α -tin and β -tin crystal properties were included in the optimization because they are stable solid phases at ambient pressure. The simple cubic crystal properties were included because we found that if we did not include these properties in the optimization procedure, the simple cubic crystal was often more stable than the α -tin and β -tin crystal structures at 0 K. Other crystal structures were not explicitly included in the optimization procedure because we found that they were consistently less stable than both α -tin and β -tin.

The second contribution is composed of liquid properties, specifically densities and self-diffusion coefficients. During each step of the optimization procedure, we ran molecular dynamics simulations in the canonical ensemble (constant NVT) with the Nosé-Hoover thermostat [42,43] on two systems that contain 216 tin atoms at 773 and 1273 K. Two target liquid number densities were taken to be 0.03459 and 0.03289\AA^{-3} for 773 and 1273 K, respectively, from experimental data [44]. The simulations were run for 5.0 ps with a time step of 1.0 fs

starting from a liquid-like configuration. We computed the average external pressure acting on the cell and self-diffusion coefficients of tin atoms from the last 2.0 ps of the trajectory. We use the pressure as an indirect way to fit the densities because we are running NVT simulations at the specified target densities. The target value for the pressure is set to be 0 GPa because many of the experimental measurements of the liquid density of tin are taken at saturation conditions. Due to the fact that tin has a low vapor pressure at the temperatures at which we are performing the fit, setting the target pressure to 0 GPa is a good approximation to the saturation pressure. The target values of self-diffusion coefficients were chosen from experimental work [39] and set to be 0.50 and $1.10 \text{\AA}^2/\text{ps}$ for 773 and 1273 K, respectively. The self-diffusion coefficients were computed from mean-square displacements (MSD) using the Einstein relation (given in the ‘‘Self-diffusivity’’ subsection) for the same simulations described above.

The final contribution was included in the target function in an attempt to obtain better agreement with the experimental zero-pressure melting temperature of 505 K [45]. Before adding the contribution, we found that the melting temperature of many early versions of the new force fields tended to be low, sometimes as low as 350 K. Therefore, we added a contribution to the target function in an attempt to improve the melting temperature. Specifically, we ran simulations in the isothermal-isobaric (constant NPT) ensemble on a 216-atom β -tin structure using the Nosé-Hoover thermostat [42,43] and Nosé-Hoover barostat [46,47] at zero pressure and three different temperatures (580, 610, and 640 K as listed in Table II). We chose temperatures higher than the experimental

melting point of Sn (505 K) because bulk solid simulations can be superheated. The length of the simulations was 10 ps with a time step of 2.0 fs. We monitored the phase of each simulation by tracking the MSD: if the MSD saturated to a finite value and thus had zero slope with respect to time (corresponding to a zero diffusion coefficient) for a majority of the trajectory, the system was deemed to be solid, while if the MSD continued to rise and thus displayed a nonzero slope with respect to time (corresponding to a nonzero diffusion coefficient) the system was deemed to be liquid. The target values of the diffusivity of these simulations was zero to ensure the simulations stayed in the β -tin phase. We note that this method is not an accurate way of obtaining the melting temperature of a force field as superheating can be observed in bulk simulations. However, it provides a means to roughly estimate this property without performing expensive molecular dynamics simulations, and is therefore a useful method for tuning the melting temperature in our optimization procedure. A more accurate method to estimate the melting point will be discussed below.

As mentioned earlier, the parameters for the new MEAM force field of tin are listed in Table I along with the parameters of the Ravelo and Baskes force field. The new force field parameters were obtained by running the simulated annealing method for approximately 5000 iterations. In one iteration each parameter is individually updated in an attempt to further minimize the target function. During the optimization procedure we used relatively small system sizes (216-atom cell) and short simulation times (5–10 ps) during molecular dynamics runs in order to increase the efficiency of the optimization. Although we should expect size effects to affect the predicted properties, especially with respect to the calculated self-diffusion coefficient (as will be discussed later in the paper), the rough estimation of these properties from the runs described was found to be sufficient to tune the new MEAM force field parameters.

III. METHODS

In this section we provide details on the methods used to calculate various properties of tin from simulations using the two MEAM force fields. Comparing the results to experimental and QM data will allow us to comment on the predictive capability of each force field.

A. Solid tin

We calculated the cohesive energy, equilibrium volume, and bulk modulus of several crystal structures of tin at 0 K. The crystal structures we examined are α -tin, β -tin, face-centered cubic (fcc), body-centered cubic (bcc), simple cubic (sc), hexagonal-close-packed (hcp), and body-centered tetragonal (bct). We varied the volume of each crystal structure within two percent of the equilibrium volume in order to obtain the cohesive energy, bulk modulus, and equilibrium volume by fitting to the Murnaghan equation of state [48].

B. Melting temperature

The melting temperature at zero pressure for each force field was obtained by calculating the Helmholtz free energies of the β -tin crystal and liquid tin as a function of temperature. We

focus on the β -tin crystal because at ambient pressure it is the experimentally stable crystal phase at melting. Due to the fact that the simulations are run at conditions corresponding to zero pressure, the melting temperature is the temperature at which the Helmholtz free energy of the β -tin crystal intersects with the Helmholtz free energy of the liquid. For each phase, we calculated the Helmholtz free energy for three temperatures: 300, 400, and 500 K. The procedure used is explained below.

1. Helmholtz free energy of the β -tin crystal

Before calculating the free energy, the temperature dependence of the lattice constants of the β -tin crystal at zero pressure were calculated by first running *NPT* molecular dynamics (using the N ose-Hoover thermostat [42,43] and N ose-Hoover barostat [46,47]) at zero pressure and at the aforementioned temperatures. The anisotropic dimension of the box was allowed to fluctuate independently of the other two dimensions. The ‘‘Einstein crystal method’’ [49] was used to compute the free energy of β -tin crystal in the *NVT* ensemble using the box dimensions from the *NPT* simulations. The ideal Einstein crystal is used as the reference state for this method. It has been shown [50] that the Helmholtz free energy of a crystal can be expressed as

$$F_{\text{solid}} = F_0^{EC} + \Delta F_1 + \Delta F_2, \quad (5)$$

where F_0^{EC} is the Helmholtz free energy of the ideal Einstein crystal with the same structure as the crystal of interest. ΔF_1 is Helmholtz free energy difference between the ideal Einstein crystal and an ‘‘interacting Einstein crystal.’’ The ‘‘interacting Einstein crystal’’ is identical to the ideal Einstein crystal except that particles also interact through the force field of interest (Ravelo and Baskes MEAM or the new MEAM). The last term ΔF_2 is the Helmholtz free energy difference between the ‘‘interacting Einstein crystal’’ and the real crystal. Calculating F_{solid} using LAMMPS has been described in detail by Aragoes *et al.* [51]. However, we will briefly describe how to calculate each term based on their work.

F_0^{EC} can be calculated analytically from the following equation:

$$\begin{aligned} \frac{F_0^{EC}}{Nk_B T} &= \frac{3}{2} \left(1 - \frac{1}{N} \right) \ln \left(\frac{\beta \Lambda_E \lambda^2}{\pi} \right) \\ &+ \frac{1}{N} \ln \left(\frac{N \lambda^3}{V} \right) - \frac{3}{2N} \ln(N), \end{aligned} \quad (6)$$

where N is the number of atoms, k_B is the Boltzmann constant, T is temperature, $\beta = \frac{1}{k_B T}$, Λ_E is the harmonic spring constant, λ is the thermal de Broglie wavelength, and V is the volume. We set the harmonic spring constant to be $\Lambda_E = 7500 k_B T / \text{Å}^2$. This value was chosen following the empirical rule given by Aragoes *et al.* [51]. The authors state that a good choice of Λ_E is one that yields a value of ΔF_1 to be about $0.02 N k_B T$ higher than U_{lattice} . U_{lattice} is defined in the next paragraph.

To calculate ΔF_1 , 4000 atoms were set up in a perfect β -tin structure. Each atom was tethered to its position in the lattice by a spring with the aforementioned spring constant. A 6.5 ns molecular dynamics simulation was run in the *NVT* ensemble in which the atoms did not interact with one another,

using a time step of 0.5 fs (all following sets of simulations described in this work also used this time step). Temperature was kept constant by velocity rescaling because the N ose-Hoover thermostat yields pathological behavior for harmonic potentials [43]. The system was allowed to equilibrate during the initial 1.5 ns. During the final 5 ns of the simulation 10^5 configurations were saved. The potential energy was found not to drift from a time-independent average during the production run so the system was deemed to be in equilibrium. (This check was performed on all molecular dynamics simulation runs described in this work to ensure equilibrium was reached.) Using either the Ravelo and Baskes force field or the new MEAM force field, the potential energy of each configuration was then calculated. ΔF_1 was then calculated from

$$\frac{\Delta F_1}{k_B T} = \frac{U_{\text{lattice}}}{k_B T} - \ln \left\langle \exp \left[- \frac{(U_{\text{sol}} - U_{\text{lattice}})}{k_B T} \right] \right\rangle, \quad (7)$$

where U_{lattice} is the potential energy of the perfect lattice for a given force field, and U_{sol} is potential energy of a configuration. The angled brackets denote an ensemble average.

ΔF_2 was calculated by slowly weakening the springs that tie each atom to its initial lattice position. It can be evaluated from the following integral,

$$\Delta F_2 = - \int_0^{\Lambda_E} \langle \Delta r(t)^2 \rangle d\Lambda'_E, \quad (8)$$

where $\langle \Delta r(t)^2 \rangle$ is the mean-squared displacement of atoms at time t with respect to their initial lattice positions. The integral in Eq. (8) was evaluated using the Gaussian quadrature method. However, due to the fact that the integrand in Eq. (8) changes over several orders of magnitude during the integration, it is useful to implement a change of variables from Λ'_E to $\ln(\Lambda'_E + c)$ so that the integral can be evaluated with a reasonable number of quadrature points [49,50,52]. We chose $c = \exp(3.5)$ because it has been shown to be a good value to obtain a good estimate of the integral [49,50]. After the change of variables Eq. (8) becomes

$$\Delta F_2 = - \int_{\ln(c)}^{\ln(\Lambda_E + c)} \langle \Delta r(t)^2 \rangle (\Lambda'_E + c) d[\ln(\Lambda'_E + c)]. \quad (9)$$

The integral in Eq. (9) was evaluated using the Gaussian quadrature method with 15 values of Λ'_E (15 quadrature points). In order to ensure that 15 quadrature points were enough to evaluate the integral, Eq. (9) was also calculated with 30 quadrature points. No significant differences were observed. For each quadrature point, 4000 atoms were again set up in a perfect β -tin structure. Each atom was tethered to its position by a spring with a spring constant of Λ'_E . At each point, a 6.5 ns simulation was run in the NVT ensemble where atoms interact with one another using one of the tin force fields. Temperature was kept constant by velocity rescaling. The system was allowed to equilibrate during the initial 1.5 ns. The mean-squared displacement with respect to the initial lattice position was computed during the final 5 ns of the simulation and used to evaluate Eq. (9).

2. Helmholtz free energy of the liquid tin

Before calculating the Helmholtz free energy of the liquid, the temperature dependence of the density at zero pressure

had to be determined. This was done by performing NPT simulations. See the ‘‘Liquid density’’ subsection for more details.

The Helmholtz free energy for liquid tin was calculated using thermodynamic integration. Starting from an ideal gas reference state, the system was compressed along an isotherm to a volume V^F calculated from the NPT calculations. Next, the system was cooled down at constant volume to reach the desired state point of the liquid phase. The Helmholtz free energy can be calculated from the following equation,

$$F_{\text{liquid}} = F^{IG} + \Delta F_{\text{isothermal}} + \Delta F_{\text{isochoric}}, \quad (10)$$

where F^{IG} is the Helmholtz free energy of the ideal gas reference state, $\Delta F_{\text{isothermal}}$ is the Helmholtz free energy change due to the isothermal compression step, and $\Delta F_{\text{isochoric}}$ is the Helmholtz free energy change due to the constant-volume cooling step. F^{IG} can be calculated analytically from the expression

$$\frac{F^{IG}}{Nk_B T} = - \ln \left(\frac{V}{\lambda^3 N} \right) - 1. \quad (11)$$

For both tin force fields, the ideal gas reference state was chosen to be 6750 tin atoms at $T^{IG} = 50\,000$ K and $V^{IG} = 1.25 \times 10^8 \text{ \AA}^3$. It was found that simulations run at these conditions closely obeyed the ideal gas law. We are also confident that the temperature chosen is above the critical temperature because when we attempted to run vapor-liquid simulations (described in more detail in the ‘‘Vapor-liquid surface tension’’ subsection) at 50 000 K we did not observe a phase separation. This is important because one wants to avoid the vapor-liquid phase envelope when performing thermodynamic integration to ensure the thermodynamic path is reversible.

$\Delta F_{\text{isothermal}}$ is calculated by isothermally compressing the system and evaluating the following equation,

$$\Delta F_{\text{isothermal}} = - \int_{V^{IG}}^{V^F} P dV', \quad (12)$$

where P is the pressure. Similarly to evaluation of the Helmholtz free energy for the β -tin crystal phase, we found that the integrand in Eq. (12) varies over several orders of magnitude during the isothermal compression. If we want to evaluate the integral with the Gaussian quadrature method, we can perform a similar change of variables in order to evaluate the integral with a reasonable number of quadrature points. Equation (12) then becomes

$$\Delta F_{\text{isothermal}} = - \int_{\ln(V^{IG} + c)}^{\ln(V^F + c)} P(V' + c) d[\ln(V' + c)], \quad (13)$$

where $c = \exp(3.5)$. For each quadrature point, 6750 atoms in the liquid phase were run at constant NVT conditions. Temperature was kept constant at 50 000 K using the N ose-Hoover thermostat [42,43], while the value of the volume depended on which point of the isothermal compression was being simulated. At each point, simulations were run for 6.5 ns. Equilibration was allowed to occur for the initial 1.5 ns, while samples of the pressure were taken during the final 5 ns. 15 quadrature points were taken in order to evaluate Eq. (13). No significant differences were observed when 30 quadrature points were used to evaluate the integral.

$\Delta F_{\text{isochoric}}$ is calculated by cooling the system at constant volume and evaluating the equation

$$\Delta \left(\frac{F_{\text{isochoric}}}{T} \right) = - \int_{T^G}^{T^F} \left(\frac{E}{T^2} \right) dT', \quad (14)$$

where T^F is the final temperature after cooling and E is the total energy. Once again, it was found that integrand of Eq. (14) changes over several orders of magnitude during the integration. Using the methodology already mentioned we can transform Eq. (14) to

$$\Delta \left(\frac{F_{\text{isochoric}}}{T} \right) = - \int_{\ln(T^G+c)}^{\ln(T^F+c)} \left(\frac{E}{T^2} \right) (T' + c) d[\ln(T' + c)], \quad (15)$$

where $c = \exp(3.5)$.

At each quadrature point, 6750 atoms in the liquid phase were simulated in the NVT ensemble. Volume was kept constant at V^F while the temperature depended on which point during the isochoric cooling was being simulated. At each point temperature was maintained at T' using the N ose-Hoover thermostat [42,43] and simulations were run for 6.5 ns. Equilibration was allowed to occur for the initial 1.5 ns, while samples of the total energy were taken during the final 5 ns. 15 quadrature points were taken in order to evaluate Eq. (15). No significant differences were observed when 30 quadrature points were used.

C. Liquid structure

The structure of liquid tin is described by the radial distribution function (RDF), $g(r)$. Using the liquid densities computed from NPT simulations (described in the ‘‘Liquid density’’ subsection) we ran NVT simulations on a system of 6750 atoms at various temperatures for 7 ns. The N ose-Hoover thermostat [42,43] was used to keep temperature constant. During the last 4 ns of the simulations we took snapshots of 10^5 configurations. The configurations were then used to compute $g(r)$. Calculations were repeated for a system size of 2662 atoms to check for system size effects, and no significant differences were observed.

D. Liquid density

Liquid density was calculated from simulations at constant NPT conditions. For both force fields, simulations were run at zero pressure and various temperatures using a system of 6750 atoms. The N ose-Hoover thermostat [42,43] and N ose-Hoover barostat [46,47] were used to keep temperature and pressure constant. The simulations were equilibrated for 1.5 ns followed by a 2 ns production run. Liquid densities were calculated by taking samples of the density during the 2 ns production run. System size effects were checked by running similar calculations for a system of 2662 atoms. No significant differences in the calculated densities were observed.

E. Self-diffusivity

The calculated self-diffusion coefficient, D^{calc} , was obtained from simulations using the Einstein relation,

$$D^{\text{calc}} = \frac{1}{6} \lim_{t \rightarrow \infty} \frac{d}{dt} \langle \Delta r(t)^2 \rangle. \quad (16)$$

Here, $\langle \Delta r(t)^2 \rangle$ is the mean-squared displacement of atoms at time t .

Simulations were performed at constant NVT conditions. Temperatures were kept constant using the N ose-Hoover thermostat [42,43]. Densities for a given temperature were taken from NPT simulations at zero pressure. For both potentials, three different system sizes were used: 6750 atoms, 2662 atoms, and 1024 atoms. This was done in order to investigate the effect of system size on the calculated diffusion coefficient. An initial 1-ns-long equilibration was run, followed by a 20-ns production period. Three to five independent simulations were run at each temperature in order to collect sufficient statistics.

F. Viscosity

The shear viscosity was calculated using the Green-Kubo equation relating the shear viscosity to the integral of the stress autocorrelation function [53]:

$$\eta = \frac{V}{k_B T} \int_0^\infty \langle P_{xy}(0) P_{xy}(t) \rangle dt. \quad (17)$$

In this equation, V is the volume of the system, k_B is the Boltzmann constant, T is temperature, and $P_{xy}(t)$ are values of the off-diagonal components of the stress tensor at time t .

Improved statistics can be obtained through a modified version of this relation using all components of the stress tensor [54]. When this is done, the relation is changed to the following equation [55],

$$\eta = \frac{V}{10k_B T} \int_0^\infty \left(\sum_{\alpha\beta} \langle P_{\alpha\beta}(0) P_{\alpha\beta}(t) \rangle \right) dt, \quad (18)$$

where $\alpha\beta = xx, xy, xz, yx, yy, yz, zx, zy$, and zz . Here we have

$$P_{\alpha\beta} = (\pi_{\alpha\beta} + \pi_{\beta\alpha})/2 - \delta_{\alpha\beta} \left(\sum_{\gamma} \pi_{\gamma\gamma} \right) / 3, \quad (19)$$

where $\delta_{\alpha\beta}$ is the Kronecker delta and

$$\pi_{\alpha\beta} = \frac{1}{V} \left[\sum_j m_j v_{j\alpha} v_{j\beta} + \sum_j \sum_{k>j} (r_{j\alpha} - r_{k\alpha}) f_{jk\beta} \right]. \quad (20)$$

In this equation, m_j is the mass of atom j . The α and β components of the velocity of atom j are $v_{j\alpha}$ and $v_{j\beta}$, respectively. $r_{j\alpha}$ and $r_{k\alpha}$ are the α components of the position vectors of atom j and atom k . Finally, $f_{jk\beta}$ is the β component of the force on atom j due to atom k . The same set of simulations used to calculate the self-diffusivity were also used to calculate the viscosity.

G. Vapor-liquid surface tension

Vapor-liquid surface tension was calculated employing a direct interfacial approach. In this approach, a liquid-phase system of 6750 atoms was first equilibrated in the NVT ensemble. We found that a 2-ns-long simulation was more than enough time to achieve this. After this, one box dimension (which will be referred to as the z dimension) was

expanded to about 2.5 times its initial size. The Nse-Hoover thermostat [42,43] was used to keep temperature constant.

After the simulation box was extended in the z dimension, the simulation was equilibrated for another 1.5 ns, followed by a 2-ns production period in the NVT ensemble. After extending the z dimension of the box, the system would spontaneously separate into a liquid and a vapor phase. Using the mechanical definition of the vapor-liquid surface tension, we were able to calculate this property using the diagonal components of the stress tensor [56] as

$$\gamma = \frac{L_z}{2} [\langle P_{zz} \rangle - 0.5(\langle P_{xx} \rangle + \langle P_{yy} \rangle)]. \quad (21)$$

In this equation γ is the vapor-liquid surface tension and L_z is the length of the box in the z dimension. P_{xx} , P_{yy} , and P_{zz} are the diagonal components of the stress tensor corresponding to the x , y , and z directions respectively. Three to five independent simulations were run at each temperature in order to collect sufficient statistics. System size effects were checked by running similar calculations for a system of 2662 atoms. No significant differences in the calculated vapor-liquid surface tensions were observed.

IV. RESULTS

A. Solid tin

The structural properties of various crystal structures of tin predicted using the two MEAM force fields are presented in Table III along with experimental and QM data for comparison. We start by observing that both the Ravelo and Baskes force field and the new MEAM force field indicate that, of the crystal structures studied, α -tin is the most stable at 0 K. This is in agreement with QM calculations and should be expected since the cohesive energies of various crystal structures were used in the fitting procedure. We note for all crystal structures that

there is a discrepancy between the MEAM force fields and QM calculations with respect to the values of the cohesive energy. This is most likely due to the fact that density functional theory using the local density approximation for electron exchange and correlation as usual overbinds with respect to the experimental cohesive energy, as evidenced by the α -tin data. Aguado showed that for α -tin and β -tin, QM calculations achieve better agreement with experimental cohesive energies if a generalized gradient approximations for electron exchange and correlation is used [57]. Aguado tested several forms of the generalized gradient approximation functional and all led to the similar results. Despite the absolute error of the QM calculations reported in Table III, the energy differences between different phases of tin are captured well. For this reason, combined with the fact that the QM calculations with the local density approximation for electron exchange and correlation provides better prediction of structural properties, only QM calculations using local density approximation for electron exchange and correlation are reported in Table III.

Note that although one objective for the new MEAM force field parameter fit was to ensure that the sc crystal structure lies higher in energy than both α -tin and β -tin, we were only able to achieve half of this objective: the new force field predicts sc to lie between α -tin and β -tin in terms of stability. Also, the Ravelo and Baskes force field provides identical results for the cohesive energies for the fcc, bcc, hcp, sc, and bct crystal structures, which is unphysical. The lack of differentiation between energies of phases provides further motivation for improving the MEAM force field.

For the bulk moduli, both force fields reproduce experiment quite well for α -tin but overestimate this property for β -tin. Similarly, for the other crystal structures, both force fields overestimate the bulk modulus with respect to QM calculations.

The Ravelo and Baskes force field provides better agreement relative to the new MEAM force field for the lattice

TABLE III. Cohesive energy E_c , bulk modulus B_0 , equilibrium volume V_0 , lattice constant a , and the c/a ratio of solid tin structures. The c/a ratio indicates the ratio between two lattice vectors for anisotropic solid structures. Quantum mechanics (QM) and experimental (Exp) data are also included for comparison. The QM data are obtained from density functional theory calculations using the local density approximation for electron exchange and correlation. In the Exp/QM rows, numbers in parentheses are experimental data and italicized numbers are quantum mechanics data.

Property	Method	α	β	fcc	bcc	sc	hcp	bct
E_c (eV/atom)	Ravelo and Baskes	-3.140	-3.085	-3.080	-3.080	-3.080	-3.080	-3.080
	New MEAM	-3.219	-3.115	-3.060	-3.075	-3.129	-3.060	-3.083
	(Exp), QM	(-3.140) [35], -3.723 [57]	-3.10 [38], -3.688 [57]	-3.613 [57]	-3.618 [57]		-3.615 [57]	-3.653 [57]
B_0 (GPa)	Ravelo and Baskes	42	64	73	74	59	64	75
	New MEAM	46	66	74	75	65	64	80
	(Exp), QM	(42.617) [36], (54) [58]	(57.037) [36], (57.9) [59]	51.4 [57]	52.8 [57]		51.3 [57]	54.8 [57]
V_0 (\AA^3 /atom)	Ravelo and Baskes	34.05	28.32	28.70	28.46	28.48	33.13	28.69
	New MEAM	31.34	26.91	27.54	27.25	26.53	31.80	27.64
	(Exp), QM	(34.05) [37]	(27.07) [37], (26.65) [60]	26.54 [57]	26.01 [57]		26.24 [57]	27.09 [57]
a (\AA)	Ravelo and Baskes	6.483	5.920	4.860	3.847	3.054	4.544	3.292
	New MEAM	6.306	5.681	4.793	3.791	2.983	4.480	3.036
	(Exp), QM	(6.483) [37]	(5.831) [37], (5.8119) [60]	4.735 [57]	3.733 [57]		3.322 [57]	3.982 [57]
c/a	Ravelo and Baskes		0.546				1.631	1.608
	New MEAM		0.587				1.634	1.975
	(Exp), QM		(0.546) [37], (0.543) [60]				1.653 [57]	0.858 [57]

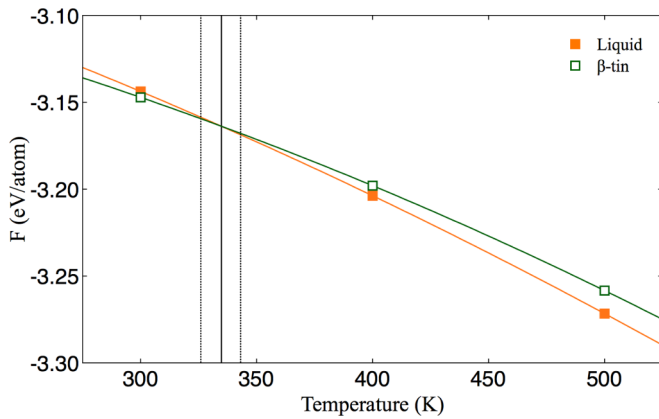


FIG. 1. Helmholtz free energy at zero pressure for the β -tin crystal and liquid tin using the Ravelo and Baskes force field. Error bars for free energy, representing the 95% confidence intervals, are smaller than the symbol size. Orange and green solid lines are fits to the data points. The black solid line represents the melting point and the black dotted lines represent the 95% confidence interval.

parameters of both α -tin and β -tin structures. Although the new MEAM force field better reproduces the equilibrium volume of the β -tin structure, it does not reproduce the experimental values for a and the c/a ratio. This is due to the fact that the new potential was optimized with the primary goal to simulate liquid tin. Less weight was placed on the β -tin structure when compared to the liquid phase during potential optimization.

B. Melting temperature

The results for the free energy calculations of the Ravelo and Baskes force field are shown in Fig. 1. For each phase, we fit a quadratic function to the points and find the intersection of these fits in order to determine the melting temperature. The intersection is shown as the solid black vertical line in the figure. Although it cannot be seen in the figure, each point has a small uncertainty associated with it, which carries over to an uncertainty in the fit. The uncertainty in the fit is not shown for clarity. Ultimately, this leads to an uncertainty in the predicted melting temperature. This is shown as black dotted lines. The predicted melting temperature for the Ravelo and Baskes force field is 334.5 ± 8.6 K. We note that this is in poor agreement with the experimental melting point of 505 K [45]. The reported melting temperature for this force field in the original work is 453 K [22]. While this number was obtained using free energy calculations, there are differences in the procedure employed for these calculations that can account for the discrepancy. In the original work, the Helmholtz free energy of the liquid phase was calculated using a different thermodynamic path than the one we used here. The path taken in their work connects the ideal gas to the real liquid by slowly turning off interactions between atoms. This path will most likely encounter a vapor-liquid phase transition and is therefore not a reversible thermodynamic path. Also, the authors calculated the Helmholtz free energy of the solid using a similar procedure (“Einstein crystal method”) to the one we described; however, it is unclear whether the authors used an appropriate thermostat when doing this. They cite that they used the N ose-Hoover thermostat [42,43]; however, as

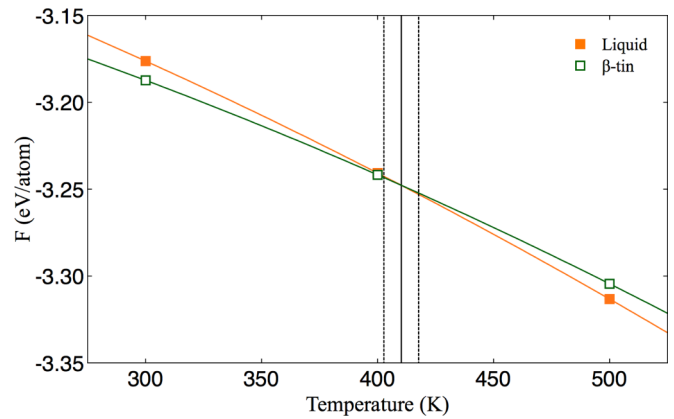


FIG. 2. Helmholtz free energy at zero pressure for the β -tin crystal and liquid tin using the new MEAM force field. Error bars for free energy, representing the 95% confidence intervals, are smaller than the symbol size. Orange and green solid lines are fits to the data points. The black solid line represents the melting point and the black dotted lines represent the 95% confidence interval.

mentioned earlier this gives rise to pathological behavior with harmonic potentials. Due to these possible sources of error in the free energy calculations of Ravelo and Baskes, we are confident that our results more accurately represent the true melting point of the potential.

The results for the free energy calculations of the new MEAM force field are shown in Fig. 2. Following the same procedure for the Ravelo and Baskes force field, we found the melting temperature for the new MEAM force field to be 410.2 ± 7.5 K. This model also underestimates the melting point, however it is closer to the experimental value than the Ravelo and Baskes force field.

We would like to note that we also performed direct interface simulations as an alternative method to calculate the melting temperature in order to provide an independent check to our free energy calculations. We found that these calculations provided slightly inconsistent results for the melting temperature. For example, using this method, the new MEAM force field yields a melting temperature of about 435 ± 3.0 K. Although this prediction gives slightly better agreement with experiment, its disagreement with the prediction from the free energy calculations raises some concern. We note that similar discrepancies have been found for solubility predictions of salts in water [61] and work is currently under way to find an explanation. For the Ravelo and Baskes force field, we found that at temperatures lower than the melting temperature, the liquid portion of the direct interface simulation crystallized into a structure different than the β -tin. This suggests that, for this force field, β -tin is not the stable crystal structure at these conditions. However, we did not attempt to investigate this behavior in more detail. For now, we note that based on our free energy calculations both force fields give poor predictions of the melting temperature if we assume the β -tin crystal structure is the stable solid phase at the conditions we are examining. The new MEAM force field provides better agreement with experimental data relative to the Ravelo and Baskes force field. This improvement can be attributed to the indirect means of fitting the melting point through the third contribution to the objective function.

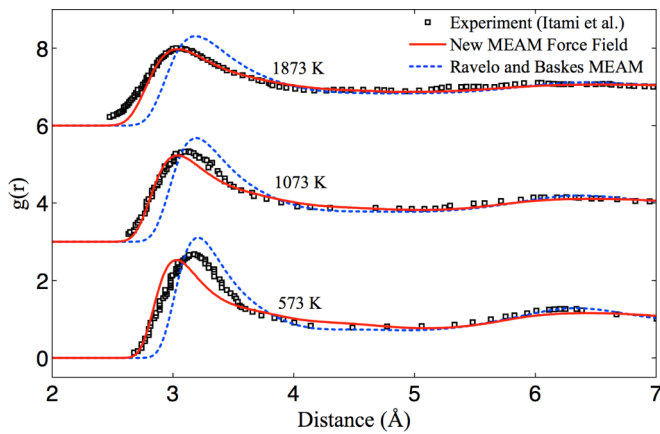


FIG. 3. A comparison of the predicted radial distribution functions $g(r)$ for the two MEAM force fields with experimental data. Experimental data are taken from Itami *et al.* [25]. The radial distribution functions at higher temperatures have been vertically shifted for clarity.

C. Liquid structure

The radial distribution functions of the two force fields along with experimental data [25] are shown in Fig. 3 for three different temperatures. At all three temperatures, the Ravelo and Baskes force field overestimates the height and position of the first peak. At 573 K the new MEAM force field underestimates the height and position of the first peak. However, this underestimation becomes less severe as the temperature increases. The peak height and position is only slightly off at 1073 K and matches perfectly at 1873 K. We point out that the RDFs were not used during the fitting procedure of the new MEAM force field, illustrating the robustness of this model for prediction of liquid-related structural properties.

D. Liquid density

The results for liquid densities are shown in Fig. 4. We compare both force fields to several sets of experimental data [44,62–64]. We note the data from Assael *et al.* [62] are recommended values determined by examining several experimental studies. It is clear that the new MEAM force field better reproduces the experimental liquid densities than the Ravelo and Baskes force field over the temperature range examined. This is not surprising, as liquid densities were used in the optimization procedure to fit the parameters of the new force field. The Ravelo and Baskes force field captures the liquid density dependence on temperature; however, it significantly underestimates experimental values.

E. Self-diffusivity

Figure 5 displays the predicted self-diffusivities along with experimental data [39,65–67]. At temperatures less than 1200 K, all four sets of experimental data are in excellent agreement. However, at temperatures greater than 1200 K some discrepancy exists between the experimental data of Itami *et al.* [66] and Bruson and Gerl [39]. One source of discrepancy may be due to the fact that the experiments by

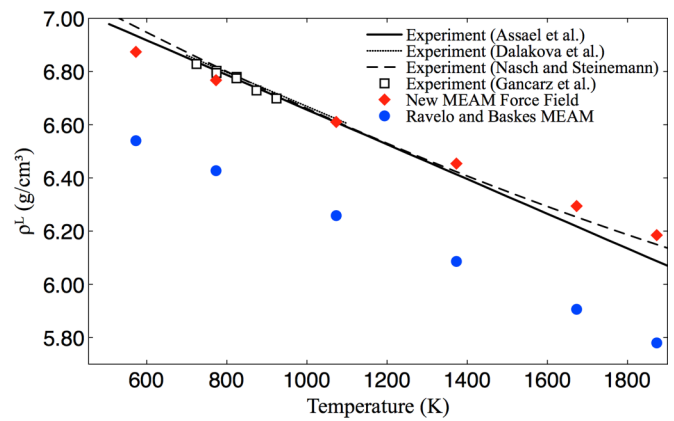


FIG. 4. A comparison of the predicted liquid densities for the two MEAM force fields with experimental data. Experimental data are taken from Assael *et al.* [62], Dalakova *et al.* [63], Nasch and Steinemann [44], and Gancarz *et al.* [64]. Error bars for simulation results, representing the 95% confidence interval, are smaller than the symbol size.

Itami *et al.* [66] were performed at microgravity conditions, while the experiments by Bruson and Gerl [39] were not. Measurements of the self-diffusion coefficient under microgravity conditions are less susceptible to convective effects [24].

The new MEAM force field better reproduces the experimental self-diffusivity than the Ravelo and Baskes MEAM force field, which consistently underestimates this property. This underestimation becomes more pronounced at higher temperatures. Although the new MEAM force field also underestimates most of the experimental data, this discrepancy is not as severe as in the case of the Ravelo and Baskes potential. As with the liquid density, the improved agreement with experimental data is not surprising, since experimental self-diffusion coefficients [39] were used in the optimization procedure.

As stated in the “Methods” section, three different system sizes were simulated in order to examine the effect on the

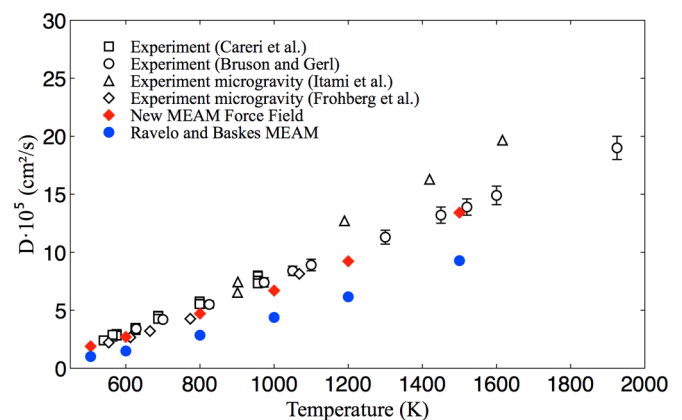


FIG. 5. A comparison of the predicted self-diffusion coefficients for the two MEAM force fields with experimental data. Experimental data are taken from Careri *et al.* [65], Bruson and Gerl [39], Itami *et al.* [66], and Frohberg *et al.* [67]. Error bars for simulation results, representing the 95% confidence interval, are smaller than the symbol size.

calculated self-diffusion coefficient. As expected, there was a significant system-size effect; however, there are two methods that can be used to correct for this. The first is to calculate the diffusion coefficient at several different system sizes and extrapolate to infinite system size ($\frac{1}{L} = 0$ where L is the box length). The second option is to use the size correction introduced by Yeh and Hummer [68]. In this procedure, one can obtain the corrected self-diffusion coefficient, D^{corr} , using the following relation,

$$D^{\text{corr}} = D^{\text{calc}} + \frac{k_B T \xi}{6\pi \eta L}. \quad (22)$$

In this equation, k_B is the Boltzmann constant, T is temperature, ξ is a constant equal to 2.837297, η is the viscosity, and L is the length of the simulated cubic cell. The viscosity is calculated from Eq. (18). We checked both correction methods and obtained statistically indistinguishable results. The results shown in Fig. 5 are from the extrapolation correction method using the three system sizes mentioned in the ‘‘Methods’’ section.

F. Viscosity

Calculated viscosities and experimental data [62,69–75] of liquid tin at different temperatures are displayed in Fig. 6. The Ravelo and Baskes force field gives predicted viscosities that consistently overestimate the experimental values shown. The new force field gives values that are in better agreement with the experimental data, although it does slightly overestimate the viscosity with respect to each experimental data set, with the exception of the data from Tan *et al.* [75]. As with their reported density data, the viscosity data from Assael *et al.* [62] are recommended values by examining several experimental studies. As was the case with calculation of the self-diffusion coefficient, three system sizes were examined in order to check for system-size effects on the calculated viscosity. However, no significant differences were observed. We note that experimental viscosities were not used during the optimization procedure when obtaining the parameters for the

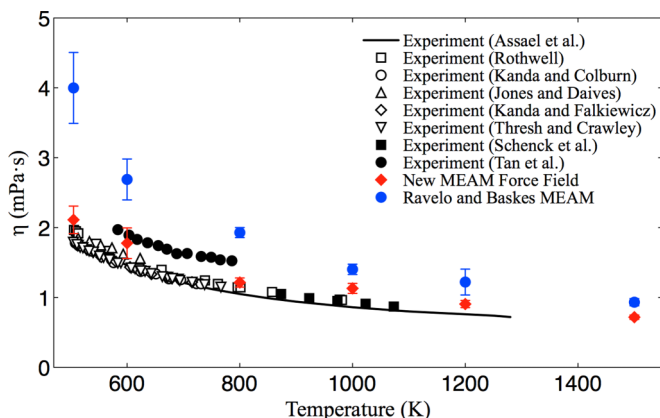


FIG. 6. A comparison of the predicted viscosities for the two MEAM force fields with experimental data. Experimental data are taken from Assael *et al.* [62], Rothwell [69], Kanda and Colburn [70], Jones and Daives [71], Kanda and Falkiewicz [72], Thresh and Crawley [73], Schenck *et al.* [74], and Tan *et al.* [75]. Error bars on simulation results represent 95% confidence intervals.

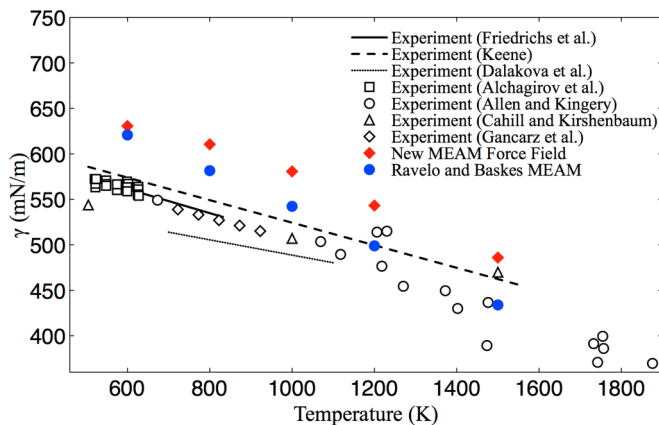


FIG. 7. A comparison of the predicted vapor-liquid surface tensions for the two MEAM force fields with experimental data. Experimental data are taken from Friedrichs *et al.* [76], Keene [77], Dalakova *et al.* [63], Alchagirov *et al.* [78], Allen and Kingery [79], Cahill and Kirshenbaum [80], and Gancarz *et al.* [64]. Error bars for simulation results, representing the 95% confidence interval, are smaller than the symbol size.

new MEAM force field. As with the liquid-phase RDFs, the new MEAM force field’s accurate prediction of the viscosity demonstrates the model’s robustness for predicting liquid tin properties.

G. Vapor-liquid surface tension

Figure 7 displays vapor-liquid surface tensions from direct interfacial simulations and several sets of experimental data [63,64,76–80]. Both the new MEAM force field and the Ravelo and Baskes force field overestimate all experimental vapor-liquid surface tension data at temperatures up to 1200 K. At this temperature, the Ravelo and Baskes potential starts to give values in agreement with some of the experimental values, while the new MEAM potential continues to overestimate this property. Both force fields seem to also overestimate the magnitude of the slope of the vapor-liquid surface tension with respect to temperature. The poor agreement of both force fields with the experimental data can be explained by the fact that the vapor-liquid surface tension was not used in the fitting procedure for either force field. We would expect better agreement if experimental values were included as part of the optimization procedure. However, the computational cost of the vapor-liquid coexistence simulations that would be required in order to compare with experimental data is too demanding to include within the optimization procedure.

V. CONCLUDING REMARKS

In this work, a critical evaluation of both an existing and a new tin MEAM force field using geometry optimization and molecular dynamics was performed. The first force field was developed by Ravelo and Baskes [22]. The second force field was developed in the current work by refitting the parameters of the aforementioned model using a simulated annealing procedure. This was done in order to obtain a force field that yields better agreement with liquid tin properties. In order to compare the two force fields, several properties were

calculated. These properties include crystal properties such as cohesive energy, bulk modulus, and equilibrium volume at 0 K. We also calculated the melting temperature, liquid density, liquid-phase RDFs, self-diffusivity, viscosity, and vapor-liquid surface tension. All properties of the force fields were compared to experimental or first-principles quantum mechanics data to assess their predictive capabilities.

For the crystal properties of tin, the Ravelo and Baskes force field provides better agreement with experimental or quantum mechanics data for most properties examined, especially with respect to α -tin and β -tin phases. For example, this force field gives better agreement with the lattice parameters for both α -tin and β -tin. The worse performance of the new MEAM force field for crystal properties is not surprising because in developing this force field, we placed more weight on the accurate prediction of liquid-phase properties. However, the new MEAM force field does predict that the α -tin crystal structure is the most stable crystal at 0 K (in agreement with quantum mechanics calculations and the Ravelo and Baskes force field) and reasonably reproduces the bulk modulus of this crystal structure.

Based on free energy calculations, both force fields provide poor predictions of the melting temperature at zero pressure. However, the new MEAM force field provides better agreement relative to the Ravelo and Baskes force field. There is also an observed discrepancy between the melting temperature calculated using free energies and the melting temperature from direct interface simulations for the new MEAM force field. The source of this discrepancy is not yet known, but ionic salts also exhibit a similar effect [61].

The new MEAM force field yields better agreement with a variety of liquid properties. For the liquid-phase RDFs, the new MEAM force field is in excellent agreement with experiments at higher temperatures. At lower temperatures, the agreement becomes worse. By contrast, at all temperatures examined, the Ravelo and Baskes force field provides poor agreement with experimental data. We point out that the liquid-phase RDFs were not used during force field optimization. Therefore, the agreement of the predictions from the new force field with experimental data highlights the robustness of the new model in terms of accurately predicting liquid properties. The new MEAM force field also better reproduces the liquid density of tin, while the Ravelo and Baskes force field consistently underestimates this property with respect to the experimental data. We reiterate that this improved agreement for the liquid density is to be expected because this property was used in the fitting procedure.

Dynamic properties of the liquid phase are also examined by calculating the self-diffusivity and viscosity. As expected, the new MEAM force field yields more accurate self-diffusion coefficients of liquid tin when compared those produced by

the Ravelo and Baskes force field. Again, this improvement is not surprising because experimental self-diffusion coefficients were part of the fitting data set. However, the new MEAM force field also agrees better with the experimental measurements for viscosity, a property not used in the optimization procedure. This again speaks to the robustness of the new force field with respect to the prediction of liquid tin properties.

Finally, we also examined how each force field predicts the vapor-liquid surface tension. Neither model agrees well with the experimental data over the entire range of temperatures examined. We attribute this to the fact that the vapor-liquid surface tension was not used when fitting the parameters for either force field.

Based on the assessment performed in this work, we conclude that the new tin MEAM force field more accurately describes the liquid phase of tin when compared to the Ravelo and Baskes force field. As with all classical force fields, the new model is not perfect. It is possible that changes to the parameter set could be made in order to achieve better agreement with other physical properties. However, due to the fact that the new force field accurately describes a wide range of liquid properties over a broad temperature range, we are confident that this potential will prove to be useful, especially with respect to simulation studies relevant to liquid metal plasma-facing materials. There may be a fundamental reason explaining why the new tin MEAM force field accurately models the liquid phase while performing poorly for the solid phases. Tin undergoes a semiconductor-metal transition between α -tin and β -tin, while the liquid phase retains many metallic characteristics. It is not clear if the MEAM formalism is robust enough to handle this type of transition; it is therefore possible that the new MEAM force field is better suited for the metallic phases of tin, especially the liquid phase. As mentioned at the beginning of this paper, this force field can be combined with a lithium force field to develop cross parameters in order to study the liquid phase of the lithium-tin alloy, or can be used to study the wetting behavior of liquid tin on relevant tokamak-related solid surfaces. It can also be used to study tin-based alloys that have the potential to be used as solders.

ACKNOWLEDGMENTS

The authors thank the Office of Fusion Energy Science, US Department of Energy, which gave support for this work under Award No. DE-SC0008598. The authors are also grateful to Michael Baskes for helpful discussions on implementing his tin force field in LAMMPS and the Terascale Infrastructure for Groundbreaking Research in Science and Engineering (TIGRESS) high-performance computing center at Princeton University for computational resources.

-
- [1] J. Glazer, *Int. Mater. Rev.* **40**, 65 (1995).
 [2] K. N. Tu, A. M. Gusak, and M. Li, *J. Appl. Phys.* **93**, 1335 (2003).
 [3] K. Zeng and K. N. Tu, *Mater. Sci. Eng., R* **38**, 55 (2002).
 [4] C. H. Miller, I. E. Anderson, and J. F. Smith, *J. Electron. Mater.* **23**, 595 (1994).

- [5] A. Hassanein, J. P. Allain, Z. Insepov, and I. Konkashbaev, *Fusion Sci. Technol.* **47**, 686 (2005).
 [6] J. W. Coenen, G. De Temmerman, G. Federici, V. Philipps, G. Sergienko, G. Strohmayer, A. Terra, B. Unterberg, T. Wegener, and D. C. M. Vanden Bekerom, *Phys. Scr.* **2014**, 014037 (2014).

- [7] J. P. Allain, D. N. Ruzic, and M. R. Hendricks, *J. Nucl. Mater.* **290-293**, 33 (2001).
- [8] R. E. Nygren, D. F. Cowgill, M. A. Ulrickson, B. E. Nelson, P. J. Fogarty, T. D. Rognlien, M. E. Rensink, A. Hassanein, S. S. Smolentsev, and M. Kotschenreuther, *Fusion Eng. Des.* **72**, 223 (2004).
- [9] C. H. Skinner, A. M. Capece, J. P. Roszell, and B. E. Koel, *J. Nucl. Mater.* **468**, 26 (2016).
- [10] M. Chen, J. Roszell, E. V. Scoullous, C. Riplinger, B. E. Koel, and E. A. Carter, *J. Phys. Chem. B* **120**, 6110 (2016).
- [11] T. W. Morgan, D. C. M. van den Bekerom, and G. D. Temmerman, *J. Nucl. Mater.* **463**, 1256 (2015).
- [12] G. G. van Eden, T. W. Morgan, D. U. B. Aussems, M. A. van den Berg, K. Bystrov, and M. C. M. van de Sanden, *Phys. Rev. Lett.* **116**, 135002 (2016).
- [13] P. Fiflis, A. Press, W. Xu, D. Andruczyk, D. Curreli, and D. N. Ruzic, *Fusion Eng. Des.* **89**, 2827 (2014).
- [14] A. G. Jackson and M. P. Hooker, *Surf. Sci.* **27**, 197 (1971).
- [15] P. Hohenberg and W. Kohn, *Phys. Rev.* **136**, B864 (1964).
- [16] W. Kohn and L. J. Sham, *Phys. Rev.* **140**, A1133 (1965).
- [17] M. S. Daw and M. I. Baskes, *Phys. Rev. B* **29**, 6443 (1984).
- [18] M. I. Baskes, *Phys. Rev. B* **46**, 2727 (1992).
- [19] J. R. Vella, F. H. Stillinger, A. Z. Panagiotopoulos, and P. G. Debenedetti, *J. Phys. Chem. B* **119**, 8960 (2015).
- [20] M. Chen, J. R. Vella, A. Z. Panagiotopoulos, P. G. Debenedetti, F. H. Stillinger, and E. A. Carter, *AIChE J.* **61**, 2841 (2015).
- [21] Z. Cui, F. Gao, Z. Cui, and J. Qu, *Modell. Simul. Mater. Sci. Eng.* **20**, 015014 (2012).
- [22] R. Ravelo and M. Baskes, *Phys. Rev. Lett.* **79**, 2482 (1997).
- [23] F. A. Sapozhnikov, G. V. Ionov, V. V. Dremov, L. Soulard, and O. Durand, *J. Phys.: Conf. Ser.* **500**, 032017 (2014).
- [24] T. Masaki, H. Aoki, S. Munejiri, Y. Ishii, and T. Itami, *J. Non-Cryst. Solids* **312-314**, 191 (2002).
- [25] T. Itami, S. Munejiri, T. Masaki, H. Aoki, Y. Ishii, T. Kamiyama, Y. Senda, F. Shimojo, and K. Hoshino, *Phys. Rev. B* **67**, 064201 (2003).
- [26] D. K. Belashchenko, *Russ. J. Phys. Chem.* **75**, 81 (2001).
- [27] M. Mouas, J.-G. Gasser, S. Hellal, B. Grosdidier, A. Makradi, and S. Belouettar, *J. Chem. Phys.* **136**, 094501 (2012).
- [28] M. Canales, L. E. González, and J. Á. Padró, *Phys. Rev. E* **50**, 3656 (1994).
- [29] L. H. Li, W. L. Wang, and B. Wei, *Comput. Mater. Sci.* **99**, 274 (2015).
- [30] P. M. Gullet, G. Wagner, A. Slepoy, M. F. Horstemeyer, H. Fang, M. Li, and M. I. Baskes, Numerical Tools for Atomistic Simulations, Tech. Rep., Sandia National Laboratories, 2004, <http://prod.sandia.gov/techlib/access-control.cgi/2003/038782.pdf>.
- [31] M. I. Baskes, *Mater. Sci. Eng. A* **261**, 165 (1999).
- [32] S. Plimpton, *J. Comput. Phys.* **117**, 1 (1995).
- [33] M. I. Baskes, J. E. Angelo, and C. L. Bisson, *Modell. Simul. Mater. Sci. Eng.* **2**, 505 (1994).
- [34] S. Kirkpatrick, C. D. Gelatt Jr., and M. P. Vecchi, *Science* **220**, 671 (1983).
- [35] C. Kittel, *Introduction to Solid State Physics* (Wiley, New York, 1986).
- [36] *Smithells Metal Reference Book*, edited by E. A. Brandes (Butterworths, London, 1983).
- [37] C. S. Barrett and T. B. Massalski, *Structure of Metals* (McGraw-Hill, New York, 1966).
- [38] J. Ihm and M. L. Cohen, *Phys. Rev. B* **23**, 1576 (1981).
- [39] A. Bruson and M. Gerl, *Phys. Rev. B* **21**, 5447 (1980).
- [40] E. Wigner, *Phys. Rev.* **46**, 1002 (1934).
- [41] B. H. Cheong and K. J. Chang, *Phys. Rev. B* **44**, 4103 (1991).
- [42] S. Nosé, *J. Chem. Phys.* **81**, 511 (1984).
- [43] W. G. Hoover, *Phys. Rev. A* **31**, 1695 (1985).
- [44] P. M. Nasch and S. G. Steinemann, *Phys. Chem. Liq.* **29**, 43 (1995).
- [45] S. T. Weir, M. J. Lipp, S. Falabella, G. Samudrala, and Y. K. Vohra, *J. Appl. Phys.* **111**, 123529 (2012).
- [46] W. G. Hoover, *Phys. Rev. A* **34**, 2499 (1986).
- [47] S. Melchionna, G. Ciccotti, and B. L. Holian, *Mol. Phys.* **78**, 533 (1993).
- [48] F. D. Murnaghan, *Proc. Natl. Acad. Sci. USA* **30**, 244 (1944).
- [49] D. Frenkel and A. J. C. Ladd, *J. Chem. Phys.* **81**, 3188 (1984).
- [50] C. Vega, E. Sanz, J. L. F. Abascal, and E. G. Noya, *J. Phys.: Condens. Matter* **20**, 153101 (2008).
- [51] J. L. Aragones, C. Valeriani, and C. Vega, *J. Chem. Phys.* **137**, 146101 (2012).
- [52] D. Frenkel and B. Smit, *Understanding Molecular Simulation*, 2nd ed. (Academic Press, San Diego, 2002).
- [53] J. P. Hansen and I. R. McDonald, *Theory of Simple Liquids*, 2nd ed. (Academic Press, Waltham, MA, 1986).
- [54] P. J. Daivis and D. J. Evans, *J. Chem. Phys.* **100**, 541 (1994).
- [55] S. H. Lee and T. Chang, *Bull. Korean Chem. Soc.* **24**, 1590 (2003).
- [56] J. S. Rowlinson and B. Widom, *Molecular Theory of Capillarity* (Clarendon Press, Oxford, 1982).
- [57] A. Aguado, *Phys. Rev. B* **67**, 212104 (2003).
- [58] C. J. Buchenauer, M. Cardona, and F. H. Pollack, *Phys. Rev. B* **3**, 1243 (1971).
- [59] S. N. Vaidya and G. C. Kennedy, *J. Phys. Chem. Solids* **31**, 2329 (1970).
- [60] J. A. Rayne and B. S. Chandrasekhar, *Phys. Rev.* **120**, 1658 (1960).
- [61] I. Nezbeda, F. Moučka, and W. R. Smith, *Mol. Phys.* **114**, 1665 (2016).
- [62] M. J. Assael, A. E. Kalyva, K. D. Antoniadis, R. M. Banish, I. Egry, J. Wu, E. Kaschnitz, and W. A. Wakeham, *J. Phys. Chem. Ref. Data* **39**, 033105 (2010).
- [63] N. V. Dalakova, K. M. Elekoeva, A. Z. Kashezhev, A. R. Manukyants, A. D. Prokhorenko, M. Kh. Ponezhev, and V. A. Sozaev, *J. Surf. Invest.: X-Ray, Synchrotron Neutron Tech.* **8**, 360 (2014).
- [64] T. Gancarz, Z. Moser, W. Gašior, J. Pstruś, and H. Henein, *Int. J. Thermophys.* **32**, 1210 (2011).
- [65] G. Careri, A. Paoletti, and M. Vicentini, *Nuovo Cimento* **10**, 1088 (1958).
- [66] T. Itami, H. Aoki, M. Kaneko, M. Uchida, A. Shisa, S. Amano, O. Odawara, T. Masaki, H. Oda, T. Ooida, and S. Yoda, *J. Japan Soc. Micrograv. Appl.* **15**, 225 (1998).
- [67] G. Froberg, K. H. Kraatz, and H. Weber, in *Proceedings of the 6th European Symposium on Materials Sciences under Microgravity Conditions, Bordeaux, France, ESA SP-256* (ESA, Paris, 1987).

- [68] I. C. Yeh and G. Hummer, *J. Phys. Chem. B* **108**, 15873 (2004).
- [69] E. Rothwell, *J. Inst. Met.* **90**, 389 (1961-1962).
- [70] F. A. Kanda and R. P. Coburn, *Phys. Chem. Liq.* **1**, 159 (1968).
- [71] W. R. D. Jones and J. B. Davies, *J. Inst. Met.* **86**, 164 (1957-1958).
- [72] F. A. Kanda and M. J. Falkiewicz, *High Temp. Sci.* **5**, 252 (1973).
- [73] H. R. Thresh and A. F. Crawley, *Metall. Trans.* **1**, 1531 (1970).
- [74] H. Schenck, M. G. Froberg, and K. Hoffmann, *Archiv für das Eisenhüttenwesen* **34**, 93 (1963).
- [75] M. Tan, B. Xiufang, X. Xianying, Z. Yanning, G. Jing, and S. Baoan, *Physica B* **387**, 1 (1963).
- [76] H. A. Friedrichs, L. W. Ronkow, and Y. Zhou, *Steel Research* **68**, 209 (1997).
- [77] B. J. Keene, *Int. Mater. Rev.* **38**, 157 (1993).
- [78] B. B. Alchagirov, O. I. Kurshev, and T. M. Taova, *Russ. J. Phys. Chem. A* **81**, 1281 (2007).
- [79] B. C. Allen and W. D. Kingery, *Trans. Am. Inst. Min. Metall. Eng.* **215**, 30 (1959).
- [80] J. A. Cahill and A. D. Kirshenbaum, *J. Inorg. Nucl. Chem.* **26**, 206 (1964).
- [81] See Supplemental Material at <http://link.aps.org/supplemental/10.1103/PhysRevB.95.064202> for the LAMMPS files implementing the force fields used in this work.